Nanoparticle movement: Plasmonic forces and physical constraints

P.E. Batson [a,*], A. Reyes-Coronado [b], R.G. Barrera [c], A. Rivacoba [b,d], P.M. Echenique [b,d], J. Aizpurua [b,d]

[a] Institute for Advanced Materials, Devices, and Nanotechnology, Rutgers University, Piscataway, NJ 08854, USA
[b] Donostia International Physics Center, "DIPC", Donostia-San Sebastian, 20018, Spain
[c] Instituto de Física, Universidad Nacional Autónoma de México, 01000 México D.F., Mexico
[d] Universidad del Pais Vasco (UPV)/EHU, and Centro de Física de Materiales CSIC-UPV/EHU, Donostia-San Sebastian 20018, Spain

ARTICLE INFO

ABSTRACT

Nanoparticle structures observed in aberration-corrected electron microscopes exhibit many types of behavior, some of which are dominated by intrinsic conditions, unrelated to the microscope environment. Some behaviors are clearly driven by the electron beam, however, and the question arises as to whether these are similar to intrinsic mechanisms, useful for understanding nanoscale behavior, or whether they should be regarded as unwanted modification of as-built specimens. We have studied a particular kind of beam–specimen interaction – plasmon dielectric forces caused by the electric fields imposed by a passing swift electron – identifying four types of forced motion, including both attractive and repulsive forces on single nanoparticles, and coalescent and non-coalescent forces in groups of two or more nanoparticles. We suggest that these forces might be useful for deliberate electron beam guided movement of nanoparticles.

© 2012 Elsevier B.V. All rights reserved.

1. Introduction

For many years, electron microscopy in materials science followed two essentially different paths: high magnification imaging of crystalline structures, defined and guided by the conceptual development of Scherzer [1], and microbeam analysis, aimed at obtaining the composition and chemistry of small specimen regions, following the early work of Hillier and Baker [2]. During an exciting and productive time in the 1970s Albert Crewe and his group knit these two fields together by introducing concepts and instrumentation which combined structural imaging and elemental characterization in the same instrument [3,4]. Further, they demonstrated a capability to image single atoms [5], and introduced methods for understanding that imaging within the context of already existing theory [6], cementing the fundamental unity embodied in the present day Transmission Electron Microscope (TEM) and Scanning Transmission Electron Microscope (STEM). This work contributed greatly to the development of more precise, quantitative methods which today allow us to identify and locate atoms within extended structures through the use of aberration correction to produce sub-Ångstrom probes [7–9] and through advanced EELS equipment to identify the local bonding environments using Electron Energy Loss Spectroscopy (EELS) in both non-aberration-corrected [10] and aberration-corrected instrumentation [11].

Thus, the modern STEM is increasingly a quantitative tool intended to provide understanding of the relationship among structure, composition, bonding, and function. With the addition of aberration correction, this work is being extended to the investigation of structure–function relationships within small groups of atoms. A good example of this is in the recent identification of catalytic behavior of a single atom [12]. An enabling feature of the aberration corrected system is the very high contrast available in single atom signals, which allows inspection of slowly evolving atomic level processes within the microscope [7,13]. These investigations are still restricted to time scales of seconds, but it seems not too far in the future that optical excitation of a high brightness source may allow recent very high temporal resolution experiments [14,15] to be extended to the atomic level.

Recently, we discussed an ubiquitous feature of aberration corrected electron microscopy: atoms and nanoscale objects are often in motion under the electron beam [13]. While this statement may seem a bit surprising to most microscopists, it has been a prominent part of reports on small particle imaging in the past [16,17]. The movement of atoms under the electron beam is an easy finding to accept, but motion of nanoscale objects was greeted with many questions. What are the primary mechanisms that produce motion? Should electron beam driven motion be considered a damage mechanism, or a variation of naturally occurring motion, a source of additional information about the specimen? With recent additional reports of interesting movement in the microscope [18,19], these questions have become more interesting and important to address.

We have looked in detail at one type of force in order to understand a primary finding that violent coalescence of well separated nanoscale metal particles can be driven by the dielectric polarization of particle pairs by a passing swift electron. We call these plasmonic forces because much of their spectral strength lies in coupled electromagnetic fields that have plasmonic origin. But they belong to the same family of forces that hold all materials together, including London Dispersion forces, Van der Waals, Debye and other forces that are central to the dynamic behavior of molecules during self-assembly, that transport complex molecules in biology, and that enable DNA and protein measurement using nanopore structures.

2. Experimental observations

These experiments were performed in a third order aberration corrected VG Microscopes STEM, using 120 keV acceleration energy [7]. The beam current varied from 50–150 pA using a 0.8 Å beam size, which is scanned in a raster fashion to produce 200 ms exposures. Therefore one measure of beam current density is 1×10^{10} amps/m^2 in the small probe, or 1×10^4 amps/m^2 averaged over the image area of 1024×1024 pixels. These are somewhat larger than typical STEM beam current densities used in materials science, but not by large amounts.

In Fig. 1 we show a schematic summary of the interaction behavior that we have demonstrated. All of these situations can be visualized as forces arising from the interaction of particle fields that arise in response to the polarizing electric field of a passing electron. We suggest the symmetry of these fields by noting the sign of local charge fluctuations at the particle surfaces. The behavior includes, on the right, in pairs of particles (1) particle coalescence, characterized by an anti-symmetric coupling of surface plasmon response fields [13], and (2) particle separation, a result of symmetric coupling caused by a swift electron passage between two particles. On the left, forces between the passing electron and a single particle include: (3) pulling of a single nanoparticle using dipole interactions at moderate impact parameters, and (4) *pushing* of a single nanoparticle using multipole interactions at small impact parameters. The first three of these behaviors are relatively straightforward. We can easily imagine pulling a single particle by the establishment of a positive image charge within the particle in response to the negative passing electron. It is also not hard to picture an attractive, coalescence force in a two-particle system, having bi-spherical
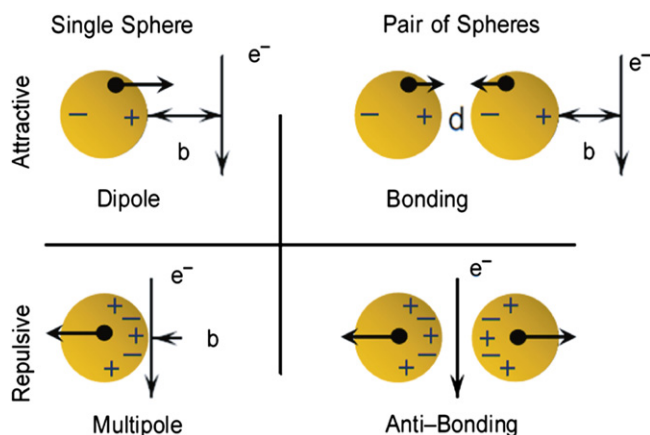

Fig. 1. Summary of observed types of plasmonic forces that are oriented perpendicular to the electron beam trajectory. They can be both attractive and repulsive in nature, and are derived from dipole and multipole interactions, depending on the impact parameter. Reproduced from [44].

symmetry. This force is a consequence of the anti-symmetric coupling of surface plasmons noticed during early development of STEM techniques [20,21] and has been discussed recently in the context of particle self assembly, where the anti-symmetric coupling is characterized as a bonding configuration [22]. Repulsion of two nanoparticles in response to an electron passing between the particles is caused by establishment of a plasmon "dark mode", having a symmetric plasmonic coupling [23]. It is little surprising that the repulsive interaction apparently overwhelms what we might expect to be an attractive, single nanoparticle response. But, perhaps in answering one surprise with another, in the fourth example, a close passage of the swift electron results in a *repulsive* force. We do not expect excitation of higher order multipoles to produce a *qualitatively* different behavior from the attractive dipole response. Based on numerical modeling that predicts the experimental finding, we speculate that response field phase shifts, which are apparent in the higher order multipoles, produce the overall force reversal.

Experimental results for these four types of movement are described in Fig. 2. In panels A–D, we show examples of particle coalescence, particle separation, single particle pulling to the left, toward the swift electron and the same particle being pushed to the right when the electron impact parameter, still on the left, is made smaller. In these panels, we identify the left edge of a scanned area with the position of the swift electron beam. This seemingly arbitrary designation is a consequence of the particular scanning strategy of the VG Microscopes STEM, used in this study. That instrument uses an analog scanning system that is synchronized with the AC power supply, to convert power line interference into image distortions, considered preferable to time varying interference when the instrument was delivered in the 1980s. Within this scheme, at the beginning of each line in the image, the electron beam pauses its scan, awaiting a synchronism pulse that is phase locked with the power line frequency. Thus, for as much as 20% of the total acquisition time, the electron beam is actually sitting unmoving at the left edge of the image. This can be verified if a small amount of contamination is allowed to build up on the specimen, as shown in Fig. 3.

Identification of this position as the effective beam position for understanding the nanoparticle behavior can be verified as shown in Fig. 4. In the inset there, we show an oblique view of the experimental scattering geometry, with the swift electron approaching from behind, passing the two sphere system. A square area denotes the x–y scan. At one edge, we show a thin elliptical area that represents where the electron beam rests before line scans in the x-direction. Finally, an angle describes the orientation of the scan relative to the line that joins the centers of the two metal spheres—or Au islands in the experiment. For several pairs of islands, we note the angle, the approximate size of the smaller of the two Au islands, and whether coalescence is rapid, slow, very slow or not at all.

From what we have described so far, if the islands support plasmonic behavior, we expect anti-symmetric coupling when the beam resting area is outside the two particle system and relatively close to the line which joins the two particles—zero angle in the summary of the data. As the angle increases to 90°, where the scan is oriented perpendicular to the two particle orientation, the propensity for coalescence decreases as described above for the "dark" anti-bonding surface plasmon modes. We have drawn a dashed line showing a cosine dependence to guide the eye, only. Notice that there is also a size dependence. Islands below 2 nm in diameter do not coalesce easily. We think that this is a consequence of interaction with the amorphous carbon substrate. Large Au metal particles (>3 nm) are well formed and metallic. They do not bond well to the substrate, and readily move under influence of plasmonic interactions with
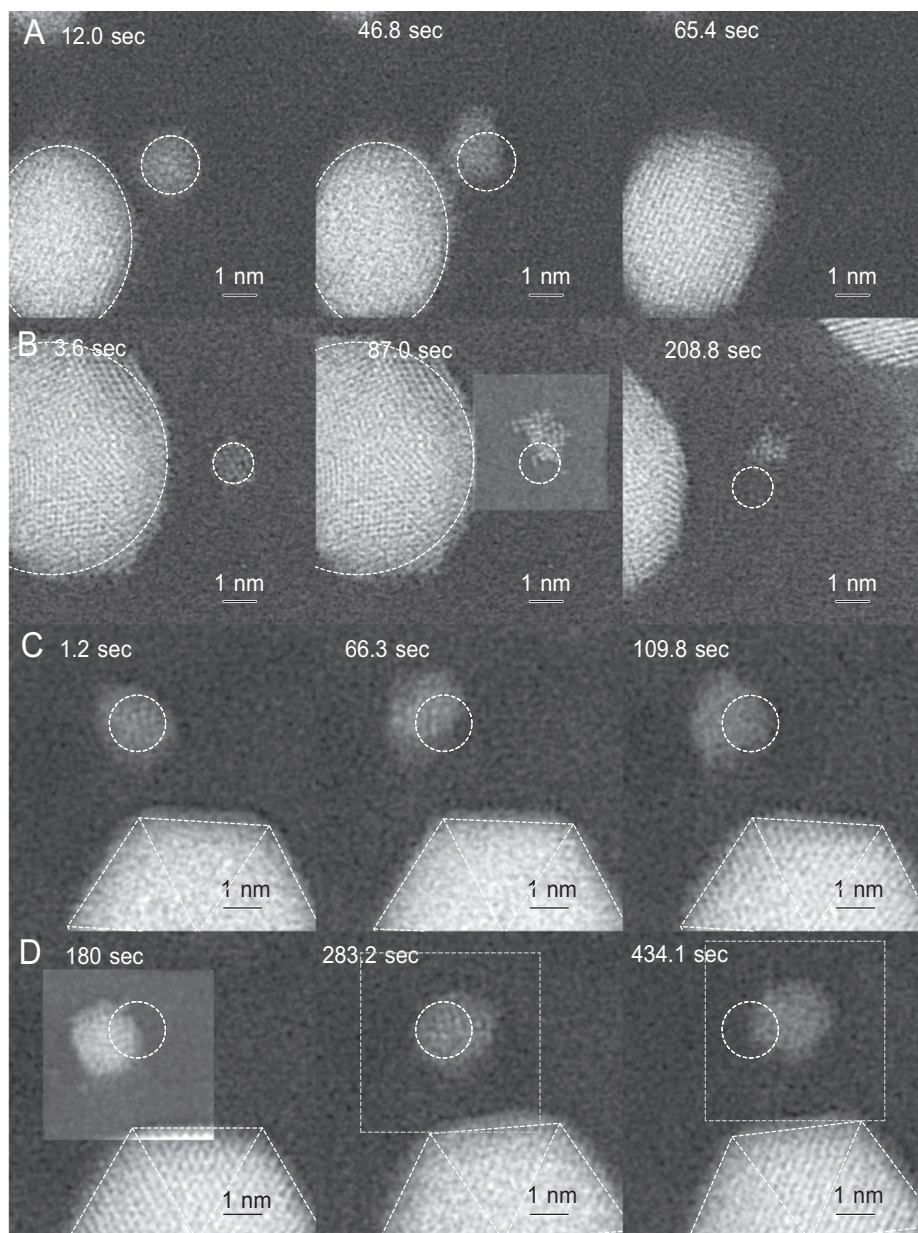
Fig. 2. Experimental observations supporting each of the four types of forces discussed with Fig. 1. In each of the examples, the effective beam position lies at the left edge of a scanned area. In (A) and (C) this is at the left edge of the field of view. In (B) and (D) this is at the left edge of the highlighted square area indicated within the field of view. In (C) and (D), the larger particle is included only to judge movement of the smaller particle. Forces between the particles in those cases are intended to be small as discussed in the text, to allow accurate judgement of the movement of the smaller particle in response to the electron beam only. Adapted from [44].

their neighbors. Small islands (< 1.5 nm), on the other hand, appear to not be fully metallic. Therefore plasmonic behavior is probably weaker, producing a smaller coalescent driving force. And the bonding of individual Au atoms with the substrate is probably stronger, producing a larger barrier to atomic motion. Fig. 4 is therefore a proof that the coalescence we observe here is driven by plasmonic response to the electron beam in particles large enough to be dominated by metallic behavior.

3. Theory

The behavior described above is apparently driven by an aloof electron beam, and so it is highly likely to be a result of polarization response fields, induced by the field of the passing electron. Other processes might also operate. For instance, electron illumination may raise the local temperature, producing instability, rotation, and structural changes [24]. Significant lateral momentum also may be transferred by electron diffraction, or secondary electron emission. Energy may be injected by inelastic losses to plasmon generation, direct knock-on processes and ionization damage. We think in this case, however, that the angular dependence evidence in Fig. 4 favors a plasmonic explanation that is anchored to the relative orientation of the two particles, and so the question we consider here is whether a plasmonic treatment can explain the observed behavior. For instance, are forces expected to be large enough to move nanoparticles; and are the various experimental behaviors summarized in Figs. 1 and 2 predicted for the experimental geometries?

We can describe the transfer of momentum from the electron beam to a nanoparticle in much the same way we describe the transfer of energy in electron energy loss scattering (EELS) using the
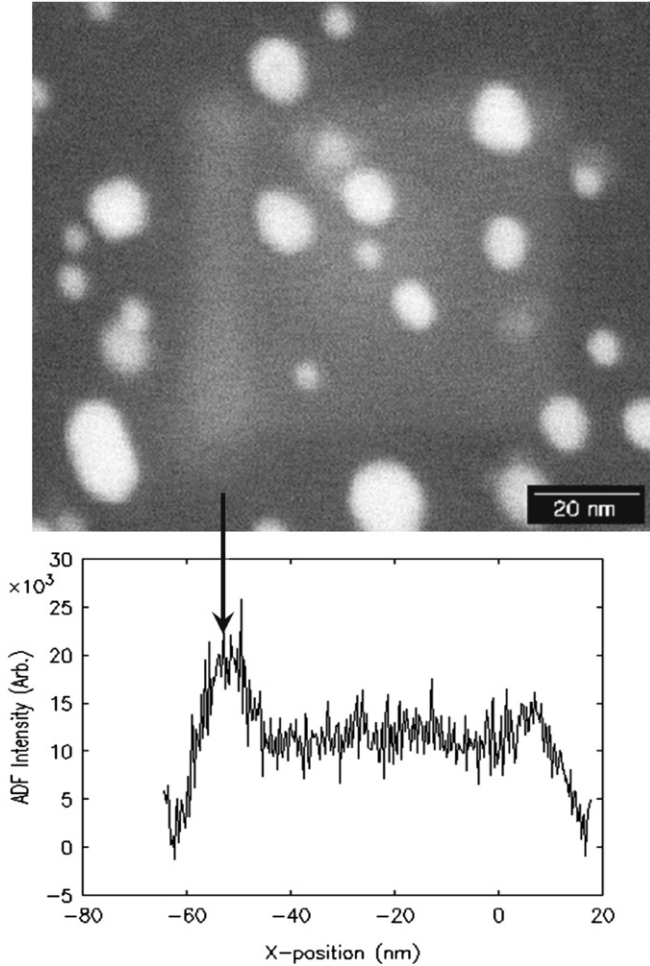
Fig. 3. Verification of the assumption of extra beam flux exists at the left edge of the scanned area. In the presence of hydrocarbons, the contaminated area defines the location of the scanned beam. It is clear in this instrument that the electron beam spends extra time at the left edge of the scanned area, awaiting a synchronization pulse before starting each line scan. This provides motivation to define the left edge as the effective position for an electron beam in visualizing the experiments defined in Fig. 1, giving results shown in Fig. 2.
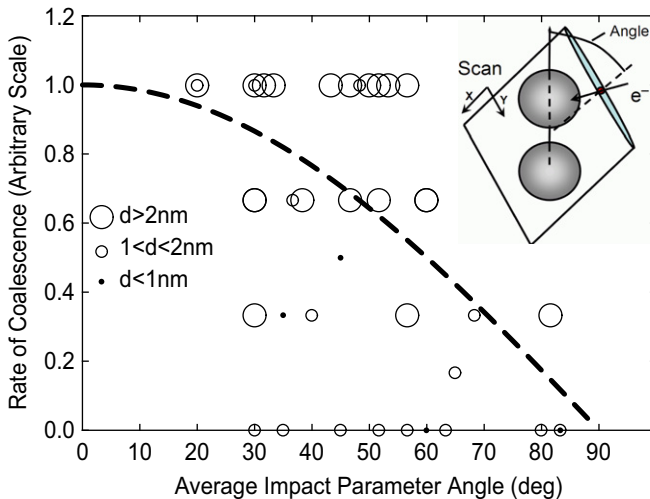

Fig. 4. Results for coalescence as a function of the angle that the scanned area makes with the line joining the two particles. The inset summarizes the experimental geometry that determines the angle. Coalescence is quickest when the orientation angle is small, and goes smoothly to zero when it approaches 90°.

classical dielectric theory. When an electron passes near a nanoparticle, it imposes a time-varying electric field. If the electron moves slowly, the particle response is proportional to the applied field and presents a conservative behavior, that is, the electron may feel a force that changes its direction, but little energy is transferred. If the electron travels faster than the Fermi velocity of electrons within the nanoparticle, then the particle polarization response lags behind the applied fields, with a resulting net field anti-parallel to the electron path, producing energy loss in the electron. The in-phase part of the response is mostly perpendicular to the electron trajectory, and stores a few times the amount of energy normally given up in inelastic losses to surface and bulk plasmons. It is called the *Wake Potential*, and can be several hundred electron volts deep for slow ions [25], but is usually only a few tenths of an electron volt deep for swift electrons [26].

The spatial extent and shape of the dielectric response is obtained in a two step process that is identical to that used in the classical dielectric theory for EELS. First the normal modes of collective excitations in the system are calculated. These include interband, single particle, bulk and surface excitations [27,28]. In a sphere, they are described by multipole modes at discrete energies controlled by the sphere size, dielectric composition and surrounding dielectric properties. In the presence of a passing electron, a straightforward boundary value problem is set up, requiring expansion of the cylindrical field of the electron, centered at a non-zero impact parameter, in terms of the multipole normal modes of the particle, centered at the origin of the particle [29]. For two interacting particles, bispherical symmetry is appropriate and has been treated also [20,30,31]. In the present case, for a passing relativistic electron, field retardation must also be considered, so the full Maxwell's Equations are used to evaluate electric and magnetic fields within the space between the particles and the swift electron [32].

This treatment includes processes that involve a direct interaction of applied electromagnetic fields with the small particles. It should also capture the coupling of those fields to photons that propagate away from the particle position, so it should reproduce a photon pressure caused by those photons as they leave [33,34]. Secondary electron emission is not included in this description, however. It might be included by considering whether part of the induced charge density includes electrons in energy state high enough to carry them over the surface workfunction, resulting in emission to the vacuum. Experimental evidence that this can happen in coincidence with surface plasmon excitation has been reported in the past [35].

The movement of a small particle in the presence of the passing electron can be obtained by evaluating the total change in momentum $\vec{P}$ of the electron due to its interaction with the particles. This momentum impulse is transferred to the particle by a mechanical force $\vec{F}_{mec}(t) \equiv d\vec{P}_{mec}/dt$, which changes with time as the swift electron passes [36–38]. We evaluate this force using the Maxwell Stress Tensor $\overleftrightarrow{T}(\vec{r};t)$ given by

$$\vec{F}_{mec}(t) = \frac{d}{dt}\vec{P}_{mec}(t) = \oint_S \overleftrightarrow{T}(\vec{r};t)\,\overrightarrow{da}, \qquad (1)$$

here $\overrightarrow{da}$ is the differential area vector normal to the closed surface S which surrounds the particle. The total impulse, given by the integration over time of the instantaneous force, can be identified with the zero frequency component of the Fourier Transform of $\vec{F}_{mec}(t)$

$$\vec{P} = \int_{-\infty}^{\infty} \vec{F}_{mec}(t)\,dt = \vec{F}_{mec}(\omega=0) = \oint_S \overleftrightarrow{T}(\vec{r};\omega=0)\,\overrightarrow{da}. \qquad (2)$$

Eq. (2) is a prescription for evaluation of the momentum change resulting from the Lorentz force imposed by sum of the applied and response electromagnetic fields in the free space

around the particles. In dyadic form, using SI system of units, the integrand involving the Maxwell Stress Tensor is given by [32]

$$
\begin{aligned}
\overleftrightarrow{T}(\vec{r};\omega=0) &= \int_{-\infty}^{\infty} \overleftrightarrow{T}(\vec{r};t)\,dt \\
&= \int_{-\infty}^{\infty} \left[\epsilon_0 \vec{E}(\vec{r};t)\otimes\vec{E}(\vec{r};t) - \frac{\epsilon_0}{2}\overleftrightarrow{I}\,\vec{E}(\vec{r};t)\cdot\vec{E}(\vec{r};t) \right. \\
&\quad \left. + \mu_0 \vec{H}(\vec{r};t)\otimes\vec{H}(\vec{r};t) - \frac{\mu_0}{2}\overleftrightarrow{I}\,\vec{H}(\vec{r};t)\cdot\vec{H}(\vec{r};t) \right] dt,
\end{aligned}
\tag{3}
$$

where $\vec{E}(\vec{r};t)$ is the electric field, $\vec{H}(\vec{r};t)$ is the magnetic field and $\otimes$ denotes the dyadic, or outer product. Thus it can be used to evaluate forces on the small particle, imposed by the total fields, calculated using the boundary value problem described above.

The forces themselves are very similar to Van der Waals and London dispersion forces, because these also result from high frequency charge density fluctuations, rather than DC fields. Thus it is useful to understand their spectral behavior. As a way of doing that, we notice that Eq. (3) involves an integral over time of products of real, time dependent functions. Therefore it can be rewritten as products of Fourier components, integrated over positive frequency space

$$
\vec{P} = \int_0^{\infty} \frac{d\vec{P}}{d\omega}\,d\omega,
\tag{4}
$$

identifying the differential momentum transfer as a function of frequency, $d\vec{P}/d\omega$ with a calculable expression that helps to identify the sign and magnitude of momentum transfer as a function of frequency [37]

$$
\begin{aligned}
\frac{d\vec{P}}{d\omega} &= \frac{1}{\pi} \oint_S \left[\epsilon_0 \vec{E}(\vec{r};\omega)\otimes\vec{E}^*(\vec{r};\omega) - \frac{\epsilon_0}{2}\overleftrightarrow{I}\,\vec{E}(\vec{r};\omega)\cdot\vec{E}^*(\vec{r};\omega) \right. \\
&\quad \left. + \mu_0 \vec{H}(\vec{r};\omega)\otimes\vec{H}^*(\vec{r};\omega) - \frac{\mu_0}{2}\overleftrightarrow{I}\,\vec{H}(\vec{r};\omega)\cdot\vec{H}^*(\vec{r};\omega) \right] \overrightarrow{da}.
\end{aligned}
\tag{5}
$$

The expression within the brackets is not the Fourier transform of $\overleftrightarrow{T}(\vec{r};t)$ but more precisely related to $\overleftrightarrow{T}(\vec{r};\omega=0)$.

In Fig. 5, we show resulting electric field intensity plots for a simple Drude metal having an electron density appropriate to aluminum ($\omega_p = 15.1$ eV and damping $\gamma = 0.15$ eV). Elements of this model are also found for the more complicated case of the Au particles, discussed elsewhere [37]. The swift electron passes through the position indicated by the black dot, in a trajectory perpendicular to the page. We show results for single (A,C) and dimer (B,D) particles, and for small (A,B) and large (C,D) energies relative to typical surface plasmon energies. Notice that the low energy results are largely dipole-like, in spite of the fact that they are assembled from several multipole modes. The multipole nature is visible in the intensity variations just inside the particle surfaces. For the single particle, this results in an attractive force for low frequency modes excited by electrons passing at large impact parameters. A striking change occurs for the higher energies, where the field is concentrated on the surface and in the bulk material near the swift electron passage. It will be seen below that this situation results in a repulsive force. We show the Drude results here for their conceptual simplicity, but plots for Au particles, using tabulated dielectric constants, embody similar behavior [37].

In Fig. 6, we show curves for $d\vec{P}_z/d\omega$ in single particles (A) and dimer pairs (B) for the Drude particles shown above. As discussed with Eq. (5), these provide evidence for the energy, or frequency, dependence of the lateral momentum transfer. In particular, we can see that the lower frequency modes, associated with the smaller angular momentum ℓ, usually produce attractive, or positive, momentum transfer—most particularly for the single particles. This attractive force and resulting momentum transfer can be understood as resulting from the creation of a positive image charge within the metal particle—the simplest method for creating a response field that results in satisfying charge and current boundary condition requirements at the surface of the particle [39–41]. For the dimers, however, many of the low frequency modes also produce negative momentum transfer—more precisely a coalescence directed momentum transfer that drives the nearer particle into its neighbor.
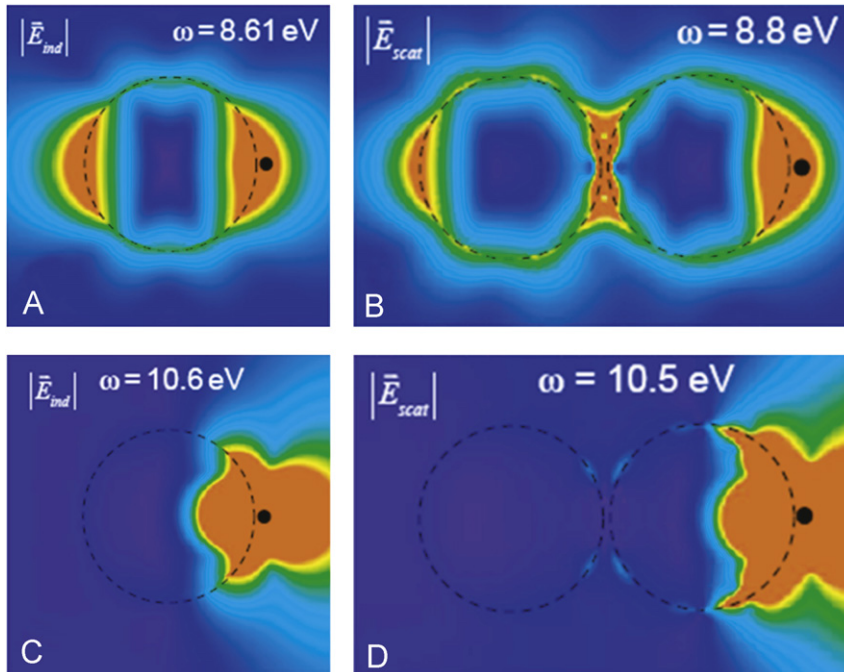

Fig. 5. Electric field intensity driven by the electron beam positioned at the single black dot, for various energies and sphere configurations. The low order modes of (A) and (B) show a strong dipole symmetry. The bispherical result of (B) shows an intense field between the two spheres, resulting in coalescence forces. In (C) and (D) higher energy modes produce repulsive forces in the single sphere case and coalescence dimer case.
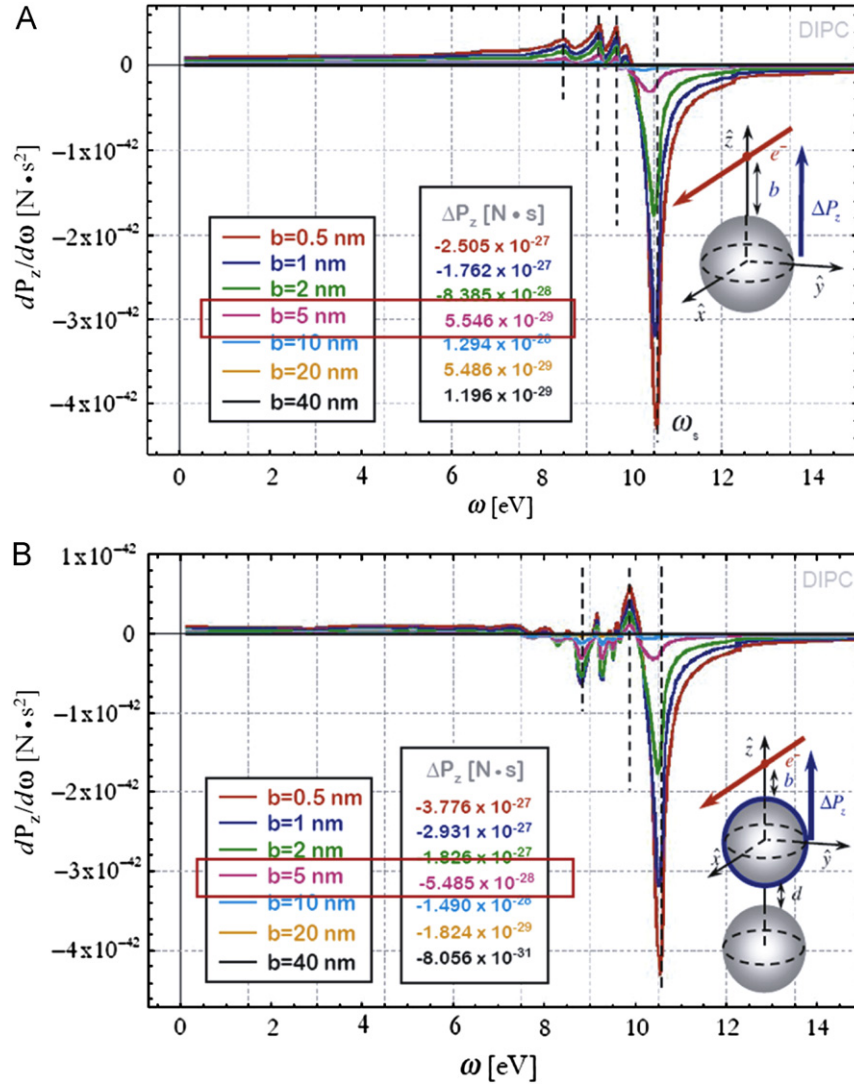
Fig. 6. Momentum transfer differential in energy, as a function of frequency ω for a single Drude sphere (A) and a sphere dimer (B). For large impact parameters, the single sphere experiences attractive forces, while for small impact parameters, those forces become repulsive. In the dimer case, the force on the sphere closest to the electron beam is always repulsive, or toward its neighboring sphere. Calculation parameters: Drude metal spheres, diameters=40 nm, $\omega_p = 15.1$ eV, $\gamma = 0.15$ eV, $d=1$ nm. (For interpretation of the references to colour in this figure legend, the reader is referred to the web version of this article.)

The higher frequency modes, corresponding to the higher multipole fields evident in Fig. 5C and D produce negative, repulsive forces. This is a non-intuitive push of single particles away from the electron beam, and an enhancement of the coalescence forces in the dimer cases. For single particles, and moderate impact parameters, small ℓ, attractive modes overcome large ℓ repulsive modes for a net attraction. At small impact parameters, the large ℓ modes are dominant, producing a net repulsive force for almost all situations. Results for Au particles, using tabulated dielectric parameters including damping, are qualitatively similar to these, but extend to higher energies due to the participation of the 4d electrons in the collective behavior of the particles.

The field magnitudes in Fig. 5 are all for passage of the swift electron at some distance outside the structure. For the particle pair, we have a qualitatively different possibility, summarized in the lower right of Fig. 1, where the electron passes between the two particles. In that case, the dimer polarization is symmetric around the electron trajectory, producing a repulsive force between the two particles. This symmetric polarization is characterized as anti-bonding because of this repulsion [22] and has been called a "dark" mode, since it does not readily couple to external photon fields [23]. This behavior further emphasizes that forces are produced even

for conservative polarization behavior. These forces largely result from the storage of energy in polarization charge within the small particle during the nearby passage of the swift electron, with a smaller contribution derived from the creation of plasmons by inelastic scattering of the electron. The experimental realization of this anti-bonding behavior is shown in Fig. 2B, where we place the left edge of the scan between the two particles, causing the smaller particle to move away from the larger one.

Integrating the differential momentum transfer, $d\vec{P}_z/d\omega$, over frequency, we can obtain the total momentum transfer, plotted as a function of impact parameter. We do that for the Au particle case in Fig. 7. Similar curves for the Drude particles are available [37]. For this result, it is clearly important to integrate over a wide enough energy range to include all important modes. In the Au case, this required using energies up to 300–400 eV. The top, red curve summarizes results as a function of impact parameter for a single 1 nm gold sphere. For large impact parameters, the momentum impulse given up to the sphere is positive, or directed toward the electron beam. Near about 0.5 nm, the impulse becomes negative, indicating a repulsive force, directed away from the electron beam. This was also noted previously in a theoretical result by García de Abajo [37]. While this interesting

behavior is apparent in the full calculations, both for Drude and for the Au materials, an understanding of the detailed mechanism is still elusive and the subject of ongoing work.

The bottom, blue curve shows results for a pair of 1 nm gold spheres, spaced 0.25 nm apart. In this case, as in Fig. 6 above, the transferred momentum is negative for all impact parameters, driving the near particle to coalesce with its neighbor. If the particle pair is separated by larger distances, the transferred momentum is shifted smoothly toward positive values, until it merges with the single particle result when the particles are far enough apart that they do not interact, summarized by the middle, green curve.

Two points in the upper left of the diagram denote the behavior for passage of the electron beam between a pair of 1 nm gold particles. A positive momentum transfer in this case means that the sphere to the right is shifted away from its neighbor. In relative terms, the three behaviors result in a strongly hierarchical set of forces—a small attractive force at large distances, a repulsive force at small distances that is about 10 times larger, and a separating force for passage of the electron between two particles that is about 10 times larger again.

We can estimate the instantaneous peak force from the change in momentum of the particle by considering the timing of passage of the swift electron. A 100 keV electron, moving at a velocity of about 0.5c, requires about 0.01 fs to pass a 1 nm metal particle. Therefore, the average force during this time interval is about $\overrightarrow{P}_z/\Delta t \approx 1 \times 10^{-29}$ N s/0.01×10^{-15} s $= 1$ pN. Referring to Fig. 7, we see that attractive forces for a single 1 nm particle are of order 0.1 pN for large impact parameters and peak around 1 pN near 1 nm, while a repulsive force for the same particle increases rapidly to values greater than 5 pN for impact parameters smaller than 0.25 nm. Pair coalescence forces are about the same for large impact parameters, but rapidly grow for small impact parameters near closely spaced particles. Repulsive forces, for particle pairs which result from passage of an electron between the particles, are as large as 60 pN for these experiments. For comparison, dielectric trapping forces, produced by large intensity gradients in finely focused beams in optical tweezers, reach values of about 70 pN for 5 MW/cm^2 light intensity [42].

If we consider a single particle to be unconstrained, floating in space perhaps, then we can work out the particle recoil velocity,
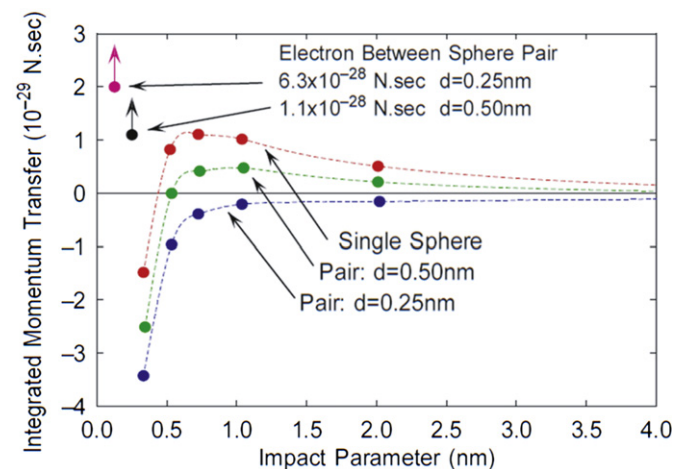
finding about 1240 nm/s for a 1 nm Au particle, with a transfer of energy of about 4×10^{-16} eV. Thus we can characterize this interaction as essentially elastic. However, as we can see from Fig. 8, the observed velocity is -0.03 nm/s for 4.5 nm impact parameter, and 0.14 nm/s for the 1.3 nm impact parameter. So this movement is not by any means unconstrained. It is likely that we do not observe the real movement, which would occur at least at thermal velocities. Using 3–5 frames/s, the best we can do is to observe quasi-stable binding positions for the Au particle. From time-to-time, governed by the beam flux density and the average energy loss given up by the passing electrons, a particle will become detached, allowing it to move to a new binding site under the influence of the electric field of the passing electron. Thus the observed movement is viscous, slow and approximately linear in time, with a slope that depends on the electron flux density and the average energy given up to the Au particle in a typical close passage. Thus the two slopes observed in Fig. 8 have roughly a 4:1 ratio, consistent with a quadrupling of flux density when the size of the scan is reduced a factor of two to change the impact parameter.

As discussed above with Fig. 2C and D, this experiment, designed to expose the influence of the electron beam on a single particle, relies on positioning the small particle near a large "fiducial" particle in such a way that the large particle does not strongly contribute to the motion of the small particle. This condition fails as the small particle moves toward large positive Z positions. We believe that this is the reason for the loss of linear motion toward the end of the experiment.

4. Constrained movement

We have seen a few instances where the nanometer Au particle behavior is clearly constrained by local configurations of other polarizable objects. We see that the particles do not accelerate, but move at more or less constant velocity while under an electron beam having fixed flux density. And we see that details of motion,
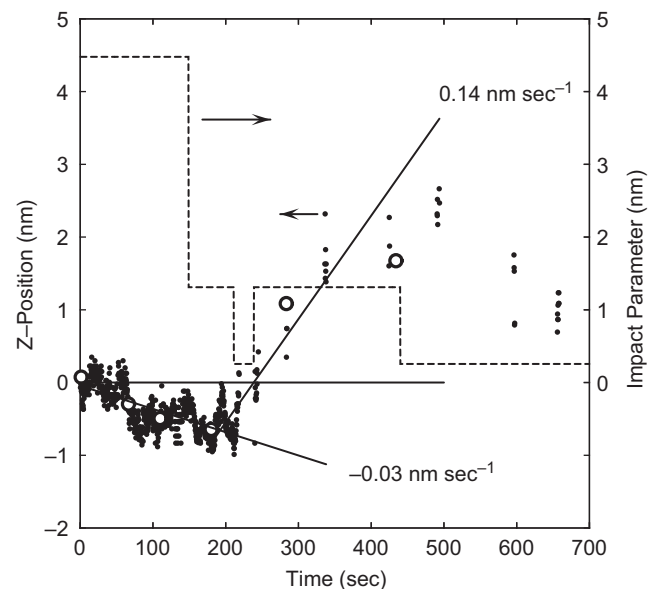
Fig. 7. Comparison of total momentum transfer along the z direction as a function of the impact parameter b, between a single small (1 nm) gold particle (top, red curve) and the top particle in a dimer of small (1 nm) gold identical particles separated by a distance $d=0.25$ nm (bottom, blue curve). For larger separations, the bottom curve shifts smoothly into the top curve (middle, green curve). Dashed lines are a guide to the eye. Model parameters are from tabulated dielectric constants for gold, as discussed in Ref. [37]. (For interpretation of the references to color in this figure caption, the reader is referred to the web version of this article.)

Fig. 8. Summary of horizontal Z-position (filled circles, ordinate on the left) of a 1.5 nm Au particle while being influenced by the electron beam. The dotted line denotes the approximate distance from the particle perimeter from the left edge of the scanned area, as discussed with Fig. 3 (ordinate on the right). The slopes of linear segments of the position curve are denoted by the straight lines. The open circles show the measured positions for images in Fig. 2C and D above.
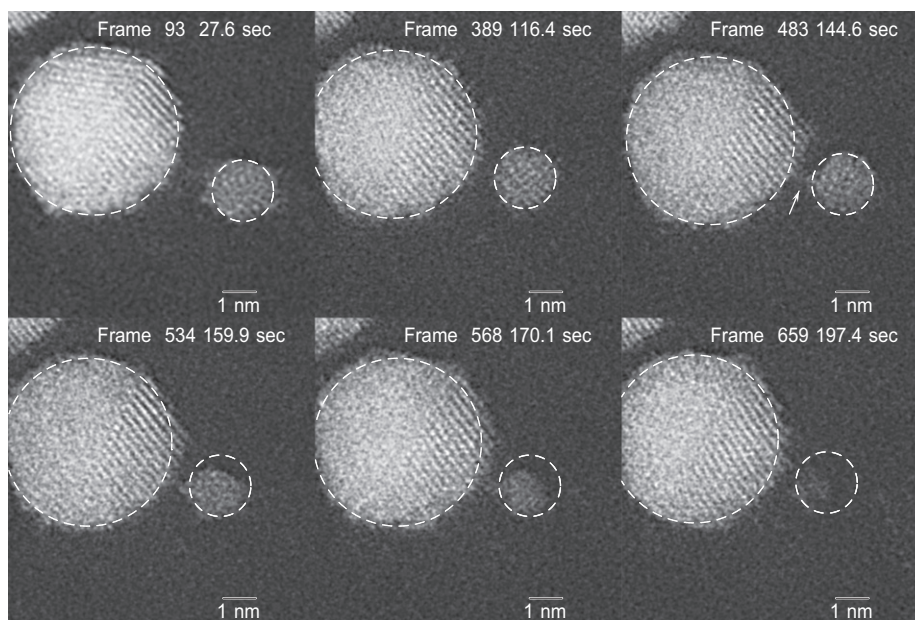
Fig. 9. Observation of coalescence in the presence of a barrier. Material transport occurs through an apparent nanopore, or narrow region with a lowered barrier to diffusion. Initially, the smaller particle is pulled toward the large sphere, but is stopped at a distance of about 0.7–0.8 nm. Atomic transport then continues in a narrow region (arrow), until most of the small particle has been transported to the larger particle.

while loosely controllable by the electron beam, also are strongly influenced by the local environment.

In Fig. 9 we show a remarkable sequence wherein particle coalescence begins to occur under influence of the electron beam as in Fig. 2A. Thus, the small particle, initially located with a 1 nm space between it and the larger particle, is induced to move to within about 0.5 nm during the first 2 min of the experiment. After that time, the small particle does not move closer. Instead, a small bridge of atoms is established between the two nanoparticles; the smaller particle loses atoms; and layers of atoms are built up on the surface of the larger nanoparticle. In the end, the smaller particle is largely depleted, but not entirely consumed. It appears, therefore, that a barrier against coalescence as a unit exists, contrary to the situation shown in Fig. 2A above.

A speculative possibility for this barrier might be a depression in the carbon support which allows more than the usual bonding of the nanoparticle atoms to the substrate, similar to enhanced bonding of atoms to atomic steps and other defects on surfaces. Trapping the smaller particle at one location in the presence of the plasmonic force would produce an internal pressure in both particles. The pressure in the smaller particle would be higher, given its smaller size and might reach 10 MPa for a 10 pN force, favoring the expulsion of atoms toward the larger particle, and transport to the lower energy environment of the larger nanoparticle. As the smaller particle is depleted, the plasmonic forces will also be reduced, ultimately stopping the process before full coalescence. This would obviously be an example of a type of Ostwald ripening, driven not by statistical arguments, but by the interaction with the electron beam.

5. Conclusions

We have discussed in some detail here mechanisms for atomic transport and nanoparticle movement under observation in the electron microscope. These observations have been made feasible by recent advances in aberration correction, but they also follow closely observations made many years ago by Crewe and his co-workers in their pioneering effort to establish Scanning Transmission Electron Microscopy as a quantitative technique that combined the best of electron optical imaging with atom specific quantitative information to produce a more complete understanding of materials at the atomic scale.

The observed behavior includes attractive forces as expected, but surprisingly, repulsive forces as well. Movement under the influence of these forces is subject to many constraints imposed by bonding the surfaces of the nanoparticles with the substrate. Thus, we think that these induced plasmonic forces are comparable to non-chemical bonding forces and therefore are useful to identify and investigate atomic and nanoscale mechanical behavior.

The observation of a strong negative force for a close passage of the fast electron brings up the possibility that an electron analog of optical tweezers might be possible [43], allowing the deliberate manipulation of molecular-sized objects in the electron microscope. This intriguing possibility has been discussed recently [18,44]. For very small objects it demands a much more detailed understanding of plasmonic behavior in systems having a limited number of electrons [45]. These results suggest that there will be many surprises in the future, as we gain greater control over the electron beam, and as we refine techniques to gain more information about atomic level systems.

Acknowledgements

References

[1] O. Scherzer, Journal of Applied Physics 20 (1949) 20.
[2] J. Hillier, R.F. Baker, Journal of Applied Physics 15 (1944) 663.

[3] A.V. Crewe, M. Isaacson, D. Johnson, Review of Scientific Instruments 40 (1969) 241.
[4] A.V. Crewe, M. Isaacson, D. Johnson, Review of Scientific Instruments 42 (1971) 411.
[5] A.V. Crewe, J. Wall, J. Langmore, Science 168 (1970) 1338.
[6] A.V. Crewe, J. Wall, Optik 30 (1970) 461.
[7] P.E. Batson, N. Dellby, O.L. Krivanek, Nature 418 (2002) 617–620.
[8] O.L. Krivanek, M.F. Chisholm, V. Nicolosi, T.J. Pennycook, G.J. Corbin, N. Dellby, M.F. Murfitt, C.S. Own, Z.S. Szilagyi, M.P. Oxley, et al., Nature 464 (2010) 571.
[9] M. Haider, S. Uhlemann, E. Schwan, H. Rose, B. Kabius, K. Urban, Nature 392 (1998) 768.
[10] P.E. Batson, Nature 366 (1993) 727.
[11] K. Suenaga, M. Koshino, Nature 468 (2010) 1088.
[12] B. Qiao, A. Wang, X. Yang, L.F. Allard, Z. Jiang, Y. Cui, J. Liu, J. Li, T. Zhang, Nature Chemistry 3 (2011) 634.
[13] P.E. Batson, Microscopy and Microanalysis 14 (2008) 89.
[14] H.S. Park, J.S. Baskin, B. Barwick, O.H. Kwon, A.H. Zewail, Ultramicroscopy 110 (2009) 7, ISSN 0304-3991.
[15] S.T. Park, M.M. Lin, A.H. Zewail, New Journal of Physics 12 (2010).
[16] L.D. Marks, Reports on Progress in Physics 57 (1994) 603.
[17] P.A. Buffat, Philosophical Transactions of the Royal Society of London A 361 (2003) 291.
[18] V.P. Oleshko, J.M. Howe, Ultramicroscopy 111 (2011) 1599, ISSN 0304-3991.
[19] O. Cretu, J.A. Rodriguez-Manzo, A. Demortiere, F. Banhart, Carbon 50 (2012) 259.
[20] P.E. Batson, Physical Review Letters 49 (1982) 936.
[21] P.E. Batson, Surface Science 156 (1985) 720.
[22] E. Prodan, C. Radloff, N.J. Halas, P. Nordlander, Science 302 (2003) 419.
[23] M.W. Chu, V. Myroshnychenko, C.H. Chen, J.P. Deng, C.Y. Mou, F.J. García de Abajo, Nano Letters 9 (2009) 399.
[24] D.J. Smith, A.K. Petford-Long, L.R. Wallenburg, J.-O. Bovin, Science 233 (1986) 872.
[25] W. Brandt, R.H. Ritchie, Nuclear Instruments and Methods in Physics Research 132 (1976) 43.
[26] P.E. Batson, Physical Review B 47 (1993) 6898.
[27] R.H. Ritchie, Physical Review 106 (1957) 874.
[28] E.A. Stern, R.A. Ferrell, Physical Review 120 (1960) 130.
[29] T.L. Ferrell, P.M. Echenique, Physical Review Letters 55 (1985) 1526.
[30] N. Zabala, A. Rivacoba, P.M. Echenique, Physical Review B 56 (1997) 7623.
[31] A. Rivacoba, N. Zabala, P. Apell, Surface Science 307–309 (Part B) (1994) 868.
[32] J.D. Jackson, Classical Electrodynamics, third ed., Wiley, New York, 1999.
[33] F.J. García de Abajo, A. Howie, Physical Review Letters 80 (1998) 5180.
[34] F.J. García de Abajo, Physical Review B 59 (1999) 3095.
[35] P. Pijper, F.J. Kruit, Physical Review B 44 (1991) 9192, ISSN 0163-1829.
[36] F.J. García de Abajo, Physical Review B 70 (2004) 115422.
[37] A. Reyes-Coronado, R.G. Barrera, P.E. Batson, P.M. Echenique, A. Rivacoba, J. Aizpurua, Physical Review B 82 (2010) 235429.
[38] A. Rivacoba, N. Zabala, J. Aizpurua, Progress on Surface Science 65 (2000) 1.
[39] A. Arnau, P.M. Echenique, Physical Review B 35 (1987) 7697.
[40] R.H. Ritchie, P.M. Echenique, F. Flores, J.R. Manson, Radiation Effects and Defects in Solids 117 (1991) 163.
[41] A. Rivacoba, P.M. Echenique, Ultramicroscopy 26 (1988) 389, ISSN 0304-3991.
[42] A.J. Hallock, P.L. Redmond, L.E. Brus, Proceedings of the National Academy of Science United States of America 102 (2005) 1280.
[43] A. Ashkin, J.M. Dziedzic, J.E. Bjorkholm, S. Chu, Optics Letters 11 (1986) 288.
[44] P.E. Batson, A. Reyes-Coronado, R.G. Barrera, A. Rivacoba, P.M. Echenique, J. Aizpurua, Nano Letters 11 (2011) 3388.
[45] J.A. Scholl, A.L. Koh, J.A. Dionne, Nature 483 (2012) 421.